optica

Planar metal/dielectric single-periodic multilayer UV flat lens: supplementary material

Ruben Maas, Jorik van de Groep, and Albert Polman*

Center for Nanophotonics, FOM Institute AMOLF, Science Park 104, 1098 XG Amsterdam, The Netherlands

**Corresponding author:polman@amolf.nl*

Published 7 June 2016

This document presents supplementary information to "Planar metal/dielectric single-periodic multilayer UV flat lens," http://dx.doi.org/10.1364/optica.3.000592.
http://dx.doi.org/10.1364/optica.3.000592.s001

1. METHODS

A. Calculations

The isofrequency contours shown in the main text are calculated using a transfer matrix method [1]. The eigenvalue $\lambda_{\pm}$ of the transfer matrix of the unit cell is related to the Bloch wavevector as $\lambda_{\pm} = \exp(\pm i k_{Bl} a)$, where a is the unit cell size. For a given geometry, the isofrequency contour is determined by calculating k_{Bl} for changing parallel wavevector k_x.

The image formed by the flat lens is analytically examined by calculating the field above the multilayer structure due to a dipole source placed below the flat lens [2]. By computing the Green's tensor for this multilayer geometry, the field above the flat lens is then found for different positions. The presence of the SiN membrane is taken into account by placing the dipole 5 nm below a 50 nm thick layer with $n = 2.2$, which corresponds to the refractive index of SiN at $\lambda_0 = 364$ nm. On top of this layer the five unit cells of the metal dielectric stack are placed, and the field is then calculated in the air region above the flat lens.

B. Fabrication

The samples were fabricated on a 50 nm thick silicon nitride membrane (Norcada NX5025A). First, a 800 nm layer of MMA was spin coated on the membrane (3000 rpm, 45 s) and baked at 150°C for 2 minutes, followed by spin coating a 70 nm layer of PMMA 950k (2000 rpm, 45 s), baked at 180° for 2 minutes.

Electron beam lithography is performed in a Raith e-LINE system, with a 20 kV acceleration voltage and a 30 μm aperture, leading to a beam current of 350 pA. Patches of 25 $\times$ 25 μm were exposed using electron beam lithography and developed with MIBK:IPA (1:3) for 90 s, followed by an IPA rinse of 30 s.

Thin films are deposited using a 10 kV electron beam physical vapor deposition tool. The film thickness is monitored during deposition using a quartz crystal. The optical properties and physical thickness of single layers deposited on separate Si substrates are experimentally determined using variable angle spectroscopic ellipsometry. The deposited layer thicknesses were used as a calibration of the quartz crystal. After this calibration the multilayer structure is deposited.

Part of the multilayer stack is lift off by soaking the sample in acetone at 50°C for one hour. The rear side of the membrane was then sputter coated with 150 nm of Cr. Using a focussed ion beam, slits of 100 nm in width were milled through this opaque Cr masking layer.

2. EFFECTIVE MEDIUM THEORY

Hyperbolic metamaterials are described by the permittivity tensor:

$$\overleftrightarrow{\epsilon} = \begin{pmatrix} \epsilon_t & 0 & 0 \\ 0 & \epsilon_t & 0 \\ 0 & 0 & \epsilon_z \end{pmatrix} \quad \textbf{(S1)}$$

where $\epsilon_t \epsilon_z < 0$. The dispersion relation is given by $k_0^2 = k_z^2/\epsilon_t + k_x^2/\epsilon_z$. For a metal dielectric stack with a deeply subwavelength unit cell size, ϵ_t and ϵ_z are given by effective medium theory as[3, 4]; $\epsilon_t = (\epsilon_d d_d + \epsilon_m d_m)/(d_d + d_m)$ and $\epsilon_z = ((\epsilon_d^{-1} d_d + \epsilon_m^{-1} d_m)/(d_d + d_m))^{-1}$. Here, d_d and d_m are the dielectric and metal layer thickness respectively. ϵ_d and ϵ_m correspond to the dielectric and metal layer permittivity.

3. DESIGN OPTIMIZATION

To evaluate the imaging performance of this metamaterial design, we investigate the precise shape of the IFC, and define the deviation from an ideal spherical IFC as:

$$D = \frac{1}{k_0} \int_0^{k_0} |\pi/a - \sqrt{k_0^2 - k_x^2} - k_{Bl}(k_x)| dk_x \quad \textbf{(S2)}$$

Where k_{Bl} is the Bloch wave vector, calculated using transfer matrix calculations. Figure S1 shows the value of D as a function

of metal and dielectric layer thickness. As can be seen, there is a wide band of combinations of d_m and d_d for which D is very low. All points on this band lead to an IFC with a curvature very close to that of free space, corresponding to an angle-independent response. This emulates the negative refraction observed in a $n = -1$ material for propagating waves, and enables the realization of a flat lens.

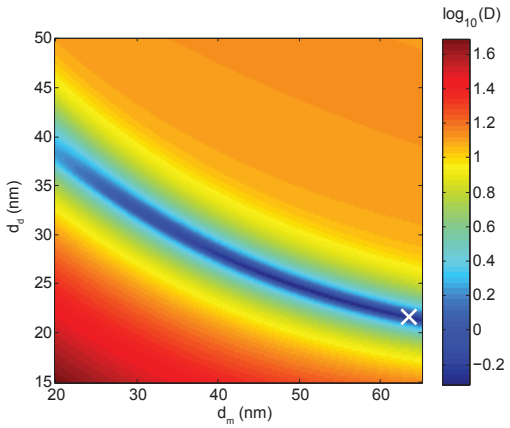

Fig. S1. Plot of deviation D from the ideal IFC curve as a function of metal (d_m) and dielectric (d_d) layer thickness. Optimization of the layer thicknesses reveals a broad band of combinations of metal and dielectric layer thicknesses achieving an isofrequency contour which is very close to ideal (blue). These structures have an IFC with a spherical shape and radius k_0. The geometry used in the calculations for Fig. 1 of the main text is indicated by the white cross

4. POYNTING VECTOR ANGLE

Analysis of the Poynting vector angle constructed from an IFC as in the main text strictly holds only for lossless and infinitely periodic structures [5]. To investigate how light refracts and propagates in a lossy, finite sized, multilayer system, we calculate the Poynting vector angle from the lateral shift of a quasi plane wave propagating through the flat lens. It has been shown that this lateral shift is proportional to the derivative of the phase of the transmitted electric field with respect to the parallel wave vector component [3, 6, 7]: $\Delta = \partial(-\arg(t(k_x)))/\partial k_x$, where the phase is given by the argument of the transmission coefficient t. The Poynting vector refraction angle is then defined as $\tan(\theta_t) = \Delta/L$, where L is the total slab thickness.

Figure S2 shows the result of this calculation. The angular response of the Poynting vector is calculated for a different number of unit cells in the range 1-10. The Poynting vector angle constructed from the IFC is shown for reference (black). As can be seen, when only one or two unit cells are considered the refraction angle deviates significantly from the curve obtained from the IFC. For a larger number of unit cells (≥ 5), both analyses yield quite similar results for angles up to 60°. This further confirms that the metamaterial structure exhibits negative refraction, even when losses and a finite structure are taken into account. The deviations in Fig. S2 for the case of a small number of unit cells are due to multiple reflections inside such a finite slab; for a larger metamaterial thickness the back reflected waves are attenuated by absorption. Note that calculating the Poynting vector angle directly from the microscopic fields will neglect the

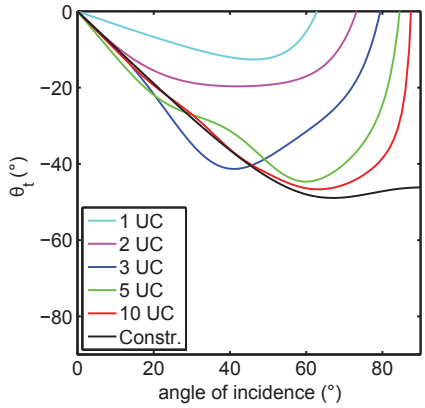

Fig. S2. Construction of the Poynting vector angle from $S \parallel \partial\omega/\partial k$ for the ideal geometry with losses (black). The colored lines correspond to the Poynting vector angle defined as $\tan(\theta_t) = \Delta/L$, where Δ is the lateral shift and L is the total slab thickness, calculated for a changing number of unit cells (UC).

macroscopic magnetization and therefore give a different result [8–10].

5. IMPACT OF LOSS ON N.A.

Here, we quantify the impact of additional material losses on the performance of our flat lens, while keeping dimensions the same as in the main text. The loss factor LF is defined as a linear scaling factor applied to the imaginary part of the permittivity of the materials from which the experimental flat lens was fabricated: Ag ($\epsilon_m = -1.762 + LF * 0.269i$), and TiO_2 ($\epsilon_d = 7.270 + LF * 0.163i$). Fig. S3a shows the Poynting vector angle constructed from the IFC, as detailed in the main text. The red, green and blue lines correspond to a loss factor of 0, 1 and 2 respectively. As can be seen, the aberrations of the lens increase with increasing losses (i.e. larger deviations from the ideal line). We define an effective numerical aperture (N.A.) corresponding to the angle of incidence where the deviation from the ideal negative refraction becomes more than 10 degrees.

Fig. S3b shows the effective N.A. as a function of the loss factor. When no losses are considered, the flat lens exhibits almost no aberrations, and therefore the N.A. is very close to 1.0. As the losses are increased, the effective N.A. gradually decreases to the value of 0.8 which we observed experimentally for $LF = 1.0$. When the losses are artificially doubled, the effective N.A. is reduced even more to approximately 0.63.

6. PHASE CONDITION

In the main text we have shown how energy refracts negatively, enabling a practical realization of a flat lens. Apart from the direction of energy propagation, indicated by the Poynting vector, the direction of phase propagation, indicated by the wave vector, is also critical to realize a flat lens as the interference at the focal point should be constructive for all angles of incidence. If we first consider a hypothetical slab of left-handed ($k \cdot S < 0$) $n = -1$ material, as Veselago did originally [11], it is easy to see how this condition is fulfilled. Figure S4 shows a sketch of the geometry. Light is emitted from a source at (x_s, z_s), and propagates with angle θ_i towards the $n = -1$ slab. Parallel

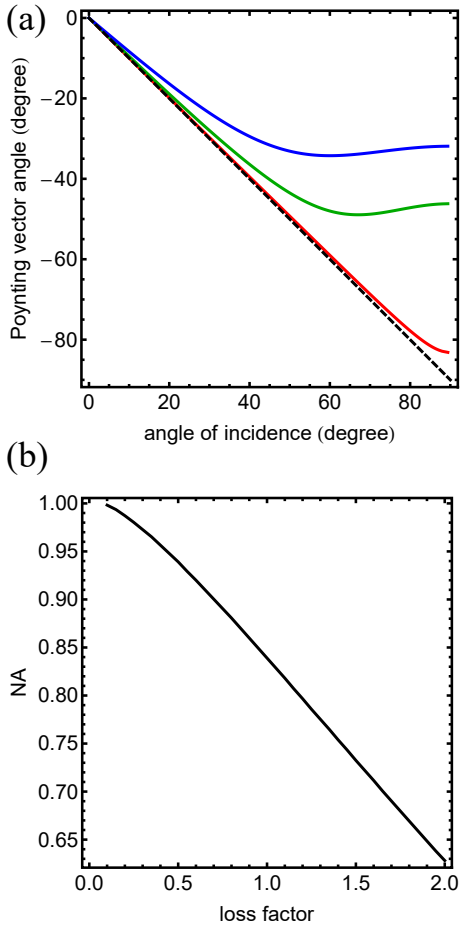

Fig. S3. **a** Constructed Poynting vector angle as a function of angle of incidence for no losses (red), a loss factor of 1 (green) and a loss factor of 2 (blue). **b** The effective N.A. of the flat lens is calculated as function of loss factor. The N.A. gradually decreases from 1.0 to 0.63 for a loss factor of 2.

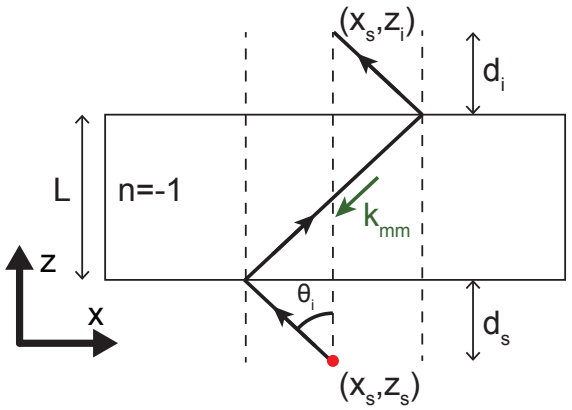

Fig. S4. Sketch of the propagation of light from a source (red) through a hypothetical $n = -1$ metamaterial slab. Negative refraction occurs over the air/$n = -1$ interfaces, and in the $n = -1$ slab the phase (indicated by k_{mm}) is propagating anti-parallel to energy (black arrows). The total slab thickness L is equal to the sum of the lens-source separation d_s and the lens-image separation d_i.

wave vector conservation over the $n = 1/n = -1$ interface completely determines refraction. From the construction it is clear that $L = d_s + d_i$, with L the lens thickness, d_s the lens-source separation, and d_i the lens-image separation. The wave vector k_{mm} inside the slab is oriented exactly anti-parallel to the direction of propagation of energy. If we decompose the phase advance, the lateral x-component drops out, as there is no net propagation in that direction. The total phase advance in the longitudinal z-direction is also zero, as the vertical component k_z changes sign inside the slab; $k_z = -\sqrt{k_0^2 - k_x^2}$. Therefore the positive phase advance $\phi_a = k_z(d_s + d_i)$ in the air region is compensated by the negative phase accrue in the $n = -1$ slab; $\phi_s = -k_z L$. Following the construction in Fig. S4, it is clear the phase at the image position (x_s, z_i) is equal to the phase at the source position (x_s, z_s): $\phi_t = \phi_a + \phi_s = 0$.

For the metamaterial studied here, $k \cdot S > 0$ for all angles (see Fig. 1d of the main text), so this metamaterial is right-handed. However, when the IFC of the multilayer geometry is spherical, the structure can fulfill the condition of constructive interference at the image position. In the wave vector diagram k_z is given by $k_z = k_{Bl} + \frac{2\pi}{a}m$. Here, k_{Bl} is the Bloch wave vector, m is an integer corresponding to the Bloch wave harmonic [12], and a is the unit cell size. In the ideal case we can simplify $k_{Bl} = \pi/a - \sqrt{k_0^2 - k_x^2}$. The total phase advance from source to image will then be: $\phi_t = k_z(d_s + d_i) + (\pi/a - \sqrt{k_0^2 - k_x^2} + \frac{2\pi}{a}m)L$. If the multilayer structure is constructed from an integer number of unit cells; $L = ja$, then $\phi_t = \pi j(1 + 2m)$. The phases in source and image thus differ by πj. As the final phase difference does not depend on the Bloch wave harmonic integer m, only considering the fundamental harmonic $m = 0$, as was done in the main text, is justified. Importantly, the phase difference is independent of angle, and therefore interference at the image position is constructive.

7. CHROMATIC ABERRATION

The experiment described in the main text was performed at a single wavelength. Here we numerically quantify the chromatic aberrations of the flat lens. We calculate the image of a dipole source, formed by the flat lens for changing wavelength of emission. The material dispersion is taken into account by using experimentally observed optical constants for the Ag and TiO_2 layers, and the change of the effective optical response of the multilayer stack is taken into account by the Green's tensor method [2].

Fig. S5a shows the change of lens-image separation with wavelength. Here, the image position is defined as the peak position along the optical axis. By changing the dipole emission wavelength with ± 5 nm, the focal length shifts by approximately ∓ 100 nm. Fig. S5b shows the change in FWHM in the lateral dimension with wavelength. As expected, the minimum FWHM is observed at the wavelength for which the flat lens design was optimized. Changing the emission wavelength by ± 5 nm increases the FWHM with approximately 5%.

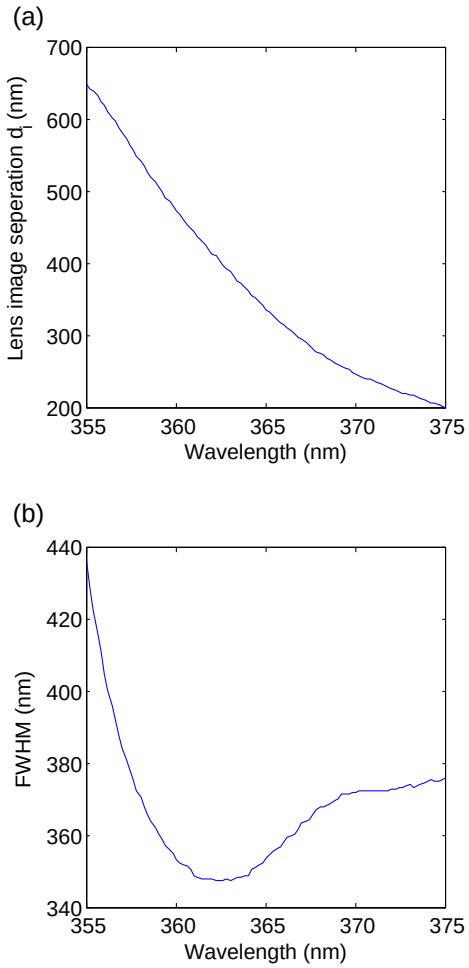

Fig. S5. a Lens-image separation d_i as a function of wavelength. This change shows the focal shift with wavelength. **b** The change of the full width half maximum (FWHM) with wavelength. As expected, we observe a minimum FWHM at the wavelength for which the design was optimized $\lambda_0 = 363.8$ nm.

REFERENCES

1. P. S. J. Russell, T. A. Birks, and F. D. Lloyd-Lucas, *Photonic Bloch Waves and Photonic Band Gaps*, Confined Electrons and Photons (Springer US, 1995).
2. M. Paulus, P. Gay-Balmaz, and O. J. F. Martin, "Accurate and efficient computation of the green's tensor for stratified media," Physical Review E **62**, 5797–5807 (2000). PRE.
3. C. Argyropoulos, N. M. Estakhri, F. Monticone, and A. Alù, "Negative refraction, gain and nonlinear effects in hyperbolic metamaterials," Opt Express **21**, 15037–47 (2013).
4. A. Poddubny, I. Iorsh, P. Belov, and Y. Kivshar, "Hyperbolic metamaterials," Nature Photonics **7**, 948–957 (2013).
5. K. Sakoda and W. T. Rhodes, *Optical Properties of Photonic Crystals* (Springer, 2003).
6. M. G. Silveirinha, "Broadband negative refraction with a crossed wire mesh," Phys. Rev. B **79**, 153109 (2009).
7. M. G. Silveirinha and A. B. Yakovlev, "Negative refraction by a uniaxial wire medium with suppressed spatial dispersion," Physical Review B **81** (2010).
8. M. G. Silveirinha, "Metamaterial homogenization approach with application to the characterization of microstructured composites with negative parameters," Physical Review B **75** (2007).
9. M. G. Silveirinha, "Poynting vector, heating rate, and stored energy in structured materials: A first-principles derivation," Physical Review B **80** (2009).
10. J. T. Costa, M. G. Silveirinha, and A. Alú, "Poynting vector in negative-index metamaterials," Physical Review B **83** (2011).
11. V. G. Veselago, "The electrodynamics of substances with simultaneously negative values of epsilon and mu," Sov. Phys. Usp. **10**, 509 (1968).
12. R. Maas, E. Verhagen, J. Parsons, and A. Polman, "Negative refractive index and higher-order harmonics in layered metallodielectric optical metamaterials," ACS Photonics **1**, 670–676 (2014).